# Biomaterials Science



#### **PAPER**



**Cite this:** *Biomater. Sci.*, 2020, **8**, 1279

Received 17th October 2019, Accepted 10th December 2019 DOI: 10.1039/c9bm01655d

rsc.li/biomaterials-science

# Improved osseointegration with rhBMP-2 intraoperatively loaded in a specifically designed 3D-printed porous Ti6Al4V vertebral implant

Teng Zhang, palaba Qingguang Wei, palaba Daoyang Fan, palaba Xiaoguang Liu, palaba Weishi Li, palaba Zhang, palaba Yun Tian, palaba Hong Cai, palaba Zheng\*b, cand Zhongjun Liu\*a, balaba Zheng\*b, cand Zheng\*b

Three-dimensional (3D)-printed porous Ti6Al4V implants are commonly used for reconstructing bone defects in the treatment of orthopaedic diseases owing to their excellent osteoconduction. However, to achieve improved therapeutic outcomes, the osteoinduction of these implants requires further improvement. The aim of this study was to investigate the combined use of recombinant human BMP-2 (rhBMP-2) with a 3D-printed artificial vertebral implant (3D-AVI) to improve the osteoinduction. Eight male Small Tail Han sheep underwent cervical corpectomy, and 3D-AVIs with or without loaded rhBMP-2 in cavities designed at the center were implanted to treat the cervical defect. Radiographic, micro-computed tomography, fluorescence labelling, and histological examination revealed that the osseointegration efficiency of the rhBMP-2 group was significantly higher than that of the blank control group. The biomechanical test results suggested that rhBMP-2 reduced the range of motion of the cervical spine and provided a more stable implant. Fluorescence observations revealed that the bone tissue grew from the periphery to the center of the 3D-AVIs, first growing into the pore space and then interlocking with the Ti6Al4V implant surface. Therefore, we successfully improved osseointegration of the 3D-AVI by loading rhBMP-2 into the cavity designed at the center of the Ti6Al4V implant, realizing earlier and more stable fixation of implants postoperatively in a simple manner. These benefits of rhBMP-2 are expected to expand the application range and reliability of 3D-printed porous Ti6Al4V implants and improve their therapeutic efficacy.

#### Introduction

Many types of spinal diseases can result in anterior column defects, especially tumours, which can lead to large bone defects. Accordingly, reconstruction of bone defects plays a major part in the treatment of certain orthopaedic diseases. The conventional approach for bone defect reconstruction involves a titanium (Ti) mesh cage, which is associated with many disadvantages such as subsidence and displacement. Moreover, a large amount of autogenous or allogeneic bone is required to fill the cage, resulting in additional side effects. As an alternative, a three-dimensional (3D)-printed porous Ti alloy implant, Ti6Al4V, was developed with demonstrated advantages in reconstructing bone defects, including an accurate shape and size with no need for bone grafting that allows

favours bone ingrowth.<sup>7</sup> Osteoconduction and osteoinduction are two fundamental characteristics of endosseous implants.<sup>8,9</sup> Although the 3D printing technique has endowed the Ti6Al4V implant with excellent osteoconduction, the osteoinduction of the Ti6Al4V surface cannot be well-controlled due to its bioinert nature.<sup>10</sup> Hence, further improvement in the osteoinduction of 3D-printed porous Ti6Al4V is indispensable to expand its applications to more complicated situations such as treatment of a poor quality bone bed or a large bone defect.<sup>11–13</sup>

for immediate stability, along with its porous feature that

To date, several methods have been proposed to augment the osseointegration of 3D-printed porous Ti6Al4V implants. One method involves the incorporation of autologous skeletal stem cells into the implants. However, aspirating autologous bone marrow from the posterior superior iliac spine intra-operatively leads to further surgical trauma in patients. <sup>12,13</sup> Other methods include surface modification by a calcium phosphate coating or layer-by-layer coatings, <sup>14,15</sup> which have short-comings of a complicated preparation process with only a limited osseointegration enhancing effect.

Exogenous recombinant human bone morphogenic protein 2 (rhBMP-2) administration has also been reported to be clini-

<sup>&</sup>lt;sup>a</sup>Department of Orthopedics, Peking University Third Hospital, Beijing 100191, People's Republic of China. E-mail: puthztlzj@163.com

<sup>&</sup>lt;sup>b</sup>Engineering Research Center of Bone and Joint Precision Medicine, Ministry of Education, Beijing 100191, People's Republic of China <sup>c</sup>Department of Materials Science and Engineering, College of Engineering, Peking University, Beijing 100871, People's Republic of China

cally useful for bone fracture repair, vertebral column tumour surgery, and other orthopaedic applications. 16-18 The time at which exogenous rhBMP-2 is administered was shown to be an important factor for fracture repair. 19 The administration of rhBMP-2 at the time of surgery (day 0) or in the early fracture healing phase (day 4) was found to enhance the periosteal and endosteal callus formation, bone mineral content, and biomechanical properties when compared to the later administration of rhBMP-2 (day 8). 20,21 Bone healing starts with the inflammatory phase, during which several biological factors, including tumour necrosis factor, transforming growth factor, BMPs, and interleukin (IL)-1β, IL-6, IL-17F, and IL-23, are released.<sup>22</sup> Thereinto, BMP-2 plays a crucial role in the initiation of bone healing. One study reported the use of BMP-2 to enhance the osseointegration of the 3D-printed porous Ti6Al4V in critical bone defects employing fibrin glue. Unfortunately, the degradation velocity of the fibrin glue was too fast to allow for BMP-2 to perform its function, and the preparation process is also too complex for practical applications.<sup>23</sup> To overcome these limitations, the aim of the present study was to establish a new and simple method for substantially improving the osseointegration of 3D-printed porous Ti6Al4V.

Specifically, we established a suitable cavity in the center of the cylindrical implant using 3D printing technology, and then tablets composed of rhBMP-2 and a carrier material (hydroxyapatite, phospholipid, and pharmagel) were inserted into the designed cavity. We validated the efficacy of the newly designed 3D-printed artificial vertebral implant (3D-AVI) using sheep, as an appropriate alternative model for evaluating spinal implants given the biomechanical similarities to the human spine. 24,25 Furthermore, as one of the highest mammalian platforms available to study osteogenesis, sheep are excellent bone healing models for the spine. <sup>26,27</sup> In contrast to the surface adsorption method, the design of the proposed material simply represents a combination of two products during surgery, thereby eliminating the need for additional Food and Drug Administration (FDA) registration. Hence, this implant will be easy to integrate into 3D-printed personalized customized surgery to improve osseointegration. The innovation of this study is as follows: firstly, the 3D printing technique has good control over the macrostructures as well as macroporous architectures of the scaffold, which is available for rhBMP-2 loading and releasing. Secondly, insertion of a tablet containing rhBMP-2 into the cavity of the 3D-printed implant during surgery is easy to operate. Finally, the release of rhBMP-2 in this work lasts for fourteen days and basically conforms to the in vivo BMP-2 release characteristic.

## Experimental

#### rhBMP-2 product preparation

Gelatine (Shanghai Naluojie Biotechnology Co., Ltd) was mixed with sterile water and autoclaved at 121 °C for 15 min using a steam sterilizer (Shanghai Shenan Medical Apparatus Instrument Co. Ltd). Hydroxyapatite (Sigma) was placed on a

clean plate and sterilized at 250 °C for 40 min using a purification cycle sterilization oven. The raw rhBMP-2 powder (Hangzhou Jiuyuan Gene Engineering Co., Ltd) was then ground with sterile water in an agate mortar. Sterilized soybean phospholipid, hydroxyapatite, and the rhBMP-2 raw powder were added to the sterilized gelatine solution, and then stirred with a thermostatic magnetic stirrer (Beijing Ruicheng Weiye Instrument and Equipment Co., Ltd) at 30 °C under 600 rpm until the solution turned to a milky white colour. Finally, the solution was injected into a freeze-dried mould with a multi-channel pipette and maintained for three days to obtain the finished product with a mass fraction of gelatine, phospholipid, and hydroxyapatite of 69.4%, 26%, and 3.6%, respectively. The rhBMP-2 used in this study is a homodimer with a molecular weight of 24 kDa.

#### Radioiodine labelling of rhBMP-2

To test the *in vitro* release, rhBMP-2 was labeled using 125I and the details are as follows. 100  $\mu$ l rhBMP2 solution (1.43 mg ml<sup>-1</sup>), 20  $\mu$ l NaOH solution of 0.1 M and 2 mCi Na 125I were added into a glass tube coated with 1,3,4,6-tetra-chloro-3 $\alpha$ ,6 $\alpha$ -diphenyl glycouril and the mixture was shaken and incubated at room temperature for 15 min. In order to separate the labeled rhBMP-2 from the uncombined 125I, the solution was dialyzed for 24 h (10 kDa MWCO Slide-A-Lyzer, Pierce), during which buffer (pH 4.5) was changed three times. The dialyzed solution was collected and concentrated in a Vivaspin ultrafiltration device (10 kDa MWCO, Sartorius AG, Germany) and 99% 125I-BMP-2 in the solution can be recycled by trichloroacetic acid (TCA). Finally, the rhBMP-2 products labeled 125I were prepared following the procedure given in the "rhBMP-2 product preparation" section.

#### In vitro rhBMP-2 release and bioactivity

The rhBMP-2 bioactivity was assayed in vitro by testing the alkaline phosphatase (ALP) activity of W20-17 cells on the samples. W20-17 cells were mouse bone marrow matrix derived and respond to the rhBMP-2 by enhanced ALP activity. In the present study, W20-17 cells (ATCC) were propagated according to the guidelines provided by the vendor, which is an ASTM standard to evaluate the activity of BMP-2 in vitro. Before the test, W20-17 cells were amplified and resuspended as homogeneous suspensions, which were equally divided and cryopreserved. Cells were resuscitated and inoculated on a 24-well plate at a density of 20 000 cells per cm<sup>2</sup> after 3 days of culture in Dulbecco's Modified Eagle's Medium (DMEM). One day later, the DMEM was replaced by the transwell containing rhBMP-2 microspheres or complexes for 7 days. In addition, cell culture medium without rhBMP-2 was used as the control to determine the basic ALP activity of W20-17 cells. To ensure the detection of ALP activity in response to rhBMP-2, the cells were cultured in transwell containing a series of concentrations (0.0, 0.01, 0.1, 1.0 and 5.0  $\mu g \text{ ml}^{-1}$ ) of rhBMP-2 as positive controls. Eventually, in vitro rhBMP-2 release kinetics and rhBMP-2 concentration in the culture medium were determined using the Gamma counter (counts per minutes).

#### In vivo rhBMP-2 release

Eighteen male SD rats (weighing 310 g–335 g; age, 12 weeks) were used in the *in vivo* rhBMP-2 release test. After shaving the hair around the right femur, the lower extremity was disinfected. After a 1 cm longitudinal skin incision was made, the femur was exposed using a periosteal detacher through intramuscular spaces. In the end, we put the rhBMP-2 product (containing 50  $\mu$ g 125I-BMP-2, a radiation dose of 4175 kBq) inside and sutured the incision. The animal was sacrificed and the radioactivity to measure the residual 125I-BMP-2 was tested (a sample size of three rats per time point).

#### Design and fabrication of the 3D-AVI

According to the cervical vertebra morphology and anatomy characteristics of the sheep, cylindrical porous Ti6Al4V implants (13-15 mm in the elliptical diameter, 18 mm in height, 5 mm in the circular hole diameter), as shown in the graphical abstract, were designed using computer assisted design (CAD) software (Magics, Materialise, Belgium), and the data were stored in the STL file format. The porous architecture was designed based on a dodecahedron unit cell with a pore size of 400-600 µm, a strut diameter of 240-320 µm and a porosity of 60%-80%. This architecture was adopted because the previous study demonstrated that the porous size at this range is beneficial for in-growth of bone and vessels. 14,23 Then, the implants were rapidly prototyped using an EBM S12 system (Acram AB, Sweden) as described previously. 14,23 According to the recommended dosage of medicine specification, one tablet containing 3 mg rhBMP-2 was inserted into the designed cavity for a total of 6 mg per sheep. To fabricate the 3D-AVIs, the 3D structure was first projected using the Mimics software, and then the acquired data were entered into an electron beam melting (EBM) S12 system (Acram AB, Sweden), which could melt the Ti6Al4V powder, and the implant was remoulded according to the CAD model. Finally, the implants were subjected to air blasting and ultrasonic cleaning to remove excess particles and pollutants.

# Establishment of a cervical corpectomy bone defect model<sup>28,29</sup> and surgical implantation

Based on the sample size calculation with the formula  $N=\frac{(Z1-\alpha/2+Z1-\beta)2\sigma 2(1+1/k)}{\delta 2}$  ( $\delta$  is the standar-

dized mean difference,  $\sigma$  is the standard deviation,  $\alpha=0.05$ ,  $\beta=0.1$ ,  $k=n_1/n_2$ ) and our previous study, <sup>30</sup> we determined that a sample size of two for the blank control group (with the asprepared 3D-AVIs implanted in the defect site) and the rhBMP-2 group (3D-AVIs loaded with rhBMP-2 implanted at the defect site) was appropriate. However, considering the potential for sample degeneracy, we used a sample size of five per group in the present study. Hence, a total of ten non-GMO, specific pathogen-free, healthy, mature male Small Tail Han Sheep (weight 48.6  $\pm$  5.7 kg; age, 17  $\pm$  4 months) underwent the anterior C3–C5 cervical corpectomy procedure and were randomly and equally assigned to the two groups according to

a two-by-two test matrix. All sheep were quarantined according to the Beijing standard for experimental sheep. The study animals were bred at the Department of Laboratory Animal Science of Peking University Health Science Center and cared for according to the principles of the Guide for the Care and Use of Laboratory Animals after obtaining the approval from the Animal Ethics Committee of Peking University Health Science Center (approval no. LA2014214).

Before surgery, the sheep were fixed in supine position for induction analgesia using propofol (4-8 mg kg<sup>-1</sup> intravenous injection) and then maintained with 1-2% isoflurane in oxygen. Penicillin (1 g intravenous) was administered prophylactically just before and at the end of surgery. Parecoxib sodium for injection (40 mg intravenous injection) was administered as postoperative analgesia. Taking the intervertebral disc as the center, we performed the corpectomy of the C3-C4 and C4-C5 cervical body through an anterior approach (Fig. 1D). Once the vertebral body and intervertebral discs were properly excised, the 3D-AVIs were placed into the prepared defect sites (Fig. 1E), followed by anterior cervical plate fixation (Fig. 1F).

Animals were individually housed and allowed free access to food and water. The ten sheep were bred together in a professional breeding room with natural lighting maintained at 20–26 °C. The sheep were fed special feed in the morning and evening and the bedding material was corncob. The sheep in the blank control group and rhBMP-2 group were treated and assessed on the same day in a blinded fashion by four separate researchers. Ultimately, only three sheep were evaluated in each group. One sheep in the blank control group was excluded owing to *Staphylococcus epidermidis* infection and one sheep in the rhBMP-2 group was excluded because of an anaesthetic complication during surgery. Radiographs of all sheep were obtained at 50 days after surgery and before sacri-

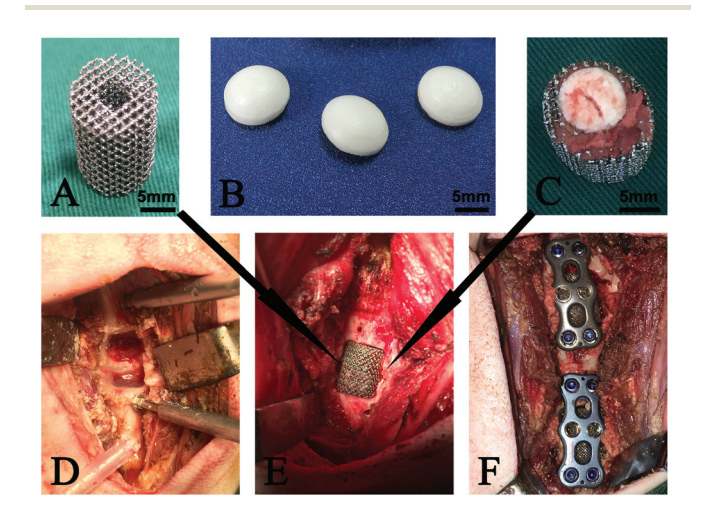


Fig. 1 Surgical implantation of the 3D-AVI into a vertebral defect in sheep. (A) The 3D-AVI used for the control group. (B) The rhBMP2 product. (C) The 3D-AVI loaded with rhBMP-2 during surgery. (D) Corpectomy of the cervical body with an anterior approach to make a bone defect model. (E) Implantation of the 3D-AVI. (F) Fixation by the anterior cervical plate.

fice to compare the bony fusion. All specimens of each group were subjected to biomechanical testing followed by microcomputed tomography (CT) and histological examination.

Cervical spinal segments (C3–C5) of all sheep were radiographically assessed for bone fusion employing X-ray and axial spiral CT scanning (Siemens, Somatom Definition Flash 64) with the following parameters: X-ray source current of 200 mA, voltage of 120 kV, 21 cm field of view, and 3 mm slice thickness. To perform the radiographs, we used intravenous injections of pentobarbital sodium (30 mg kg<sup>-1</sup>) for short-term sedation. The amount of bone formation was graded in a blinded fashion by five separate observers using a six-tiered scale (0–5) as follows: 0, no bone formation; 1, reactive bone; 2, small amount of bone formation; 3, bone formation without bridging; 4, bone formation with unilateral bridging; 5, bone formation with bilateral bridging or solid fusion mass.<sup>25</sup>

#### **Biomechanical evaluation**

The C2–C6 motion segments were thawed overnight at room temperature the day before biomechanical testing. All of the muscular tissue was resected, and the ligaments, discs, and capsules were preserved. Screws were transfixed through the C2 and C6 vertebral body and then embedded in polymethyl methacrylate for fixation on the biomechanical testing machine (MTS 858 Mini Bionix II; MTS Systems Inc., Minneapolis, MN, USA).

Three-dimensional displacement of each segment was tested employing an optical measurement system (Optotrak 3020; Northern Digital, Waterloo, Canada). Flexibility tests were performed at pure moments of 2.5 N m in the following three motion planes: flexion–extension, lateral bending to the right/left, and axial rotation to the right/left. The moment was applied at a rate of about  $0.5^{\circ}$  s<sup>-1</sup>. In general, four complete loading cycles of the process were repeated in which the first three cycles were used to reduce viscoelastic effects and the fourth cycle was used for analysis. All specimens were tested at room temperature and maintained wet using physiological saline solution. The range of motion (ROM) of the C3–C5 was tested and compared with respect to the kinematic behaviour. The ROM was defined as the angular displacement during the minimum and maximum bending moment.<sup>26</sup>

#### Micro-CT analysis

After the fixed screw plate was removed, high-resolution micro-CT was performed with an Inveon MM system (Siemens, Munich, Germany) to measure the amount and distribution of bone in each 3D-AVI. Each specimen was analysed with segmentation software, and the analysed region of interest included the bone within the 3D-AVI plus the bone proximal to it, whose boundary was manually positioned for definition. The experimenter was blinded to all groups being assessed. Three-dimensional reconstructions were made with two-dimensional images using a 3D visualization system (Inveon Research Workplace, Siemens, Munich, Germany). The bone ingrowth was determined by bone volume fraction, which was calculated as the bone volume/tissue volume ratio. Appropriate

mineralized bone phases were calculated by adjusting the threshold value (1000–3885).

#### Fluorescence labelling

To determine the osteogenesis characteristic, including the osseointegration efficiency and direction of the scaffold after implantation, in vivo sequential fluorescence labelling was performed to label the newly formed bone at different time points.<sup>31</sup> Specifically, calcein green (10 mg kg<sup>-1</sup>, Sigma, St Louis, MO, USA) and tetracycline (20 mg kg<sup>-1</sup>, Sigma) were injected intravenously at 50 and 68 days after implantation, respectively. The 3D-AVIs plus the proximal bone were harvested and fixed in 10% formalin for 2 weeks, and then dehydrated in a graded ethanol series (50%, 70%, 80%, 90%, 95%, and 100%) under vacuum conditions for 4 days. After embedding the samples in methyl methacrylate, thin slices (200-300 µm) were cut from the blocks and ground to a thickness of 100-150 µm using transverse saw cuts and a polishing machine (Exact band saw; Exact Apparatebau, Norderstedt, Germany). The osseointegration efficiency was examined with a confocal laser-scanning microscope (Leica TCS-SP8 STED 3×, Leica, Germany) at 5× magnification. The fluorescence of calcein green and tetracycline was excited sequentially by a laser beam with wavelengths of 488 nm and 405 nm, respectively. The fluorescence signals emitted were detected at 490-540 nm (calcein) or 550-610 nm (tetracycline). In addition, to investigate the osseointegration direction, we used a general fluorescence microscope (Leica, Germany) to observe the newly formed bone after calcein and tetracycline injection.

#### Histologic analysis

Following the fluorescence labelling assessment, the  $100-150~\mu m$  slices were stained with toluidine blue dye solution. Using a BioQuant Image Analysis System (BioQuant Image AnalysiCorp., Nashville, TN, USA), the available pore space of each section was normalized to 100%, and the percentage of bone ingrowth for each section was calculated. <sup>28</sup> The bone ingrowth of the entire specimen was then evaluated.

#### Statistical analysis

Data analysis was carried out using SPSS version 24.0 (IBM, Chicago, IL, USA), and data are presented as means and standard deviations. The Kolmogorov–Smirnov test was used to determine whether the continuous data were normally distributed. The percentage of bone ingrowth was compared between groups with analysis of variance with multiple comparisons. ROM data were analysed using the two-tailed Student *t*-test. *P* values <0.05 were considered statistically significant.

#### Results

#### General observations

The majority of the sheep survived the surgery and recovered without complications, except for one sheep that died from post-operative infection. The mean operative time was 92 min.

Two of the eight sheep were limp and showed weakness after the surgery, and the neurological symptoms disappeared within 3 days without any treatment.

#### In vitro rhBMP-2 release and bioactivity

As shown in Fig. 2, rhBMP-2 can facilitate ALP activity of W20-17 cells depending on the concentration. However, the ALP release is no longer increased when the concentration of rhBMP-2 reaches up to 1  $\mu g$  ml $^{-1}$ . During the first three days of the *in vitro* rhBMP-2 release test, the specimen expanded due to water absorption, resulting in a burst release of rhBMP-2. Until the third day, almost 40% rhBMP-2 was released. During the fourth day to the seventh day, the rhBMP-2 release becomes steady and 70% of the rhBMP-2 amount was released on the seventh day. Eventually, nearly all of the rhBMP-2 was released in fourteen days (Fig. 3). The rhBMP-2 products can increase ALP activity during the whole release process, indicating that the rhBMP-2 activity was stable (Fig. 4).

#### In vivo rhBMP-2 release

Due to the change in release environment, the *in vivo* rhBMP-2 release profile had a distinct difference compared with the *in vitro* rhBMP-2 release profile. *In vivo* release, 52% of the rhBMP-2 amount was released in three days after operation

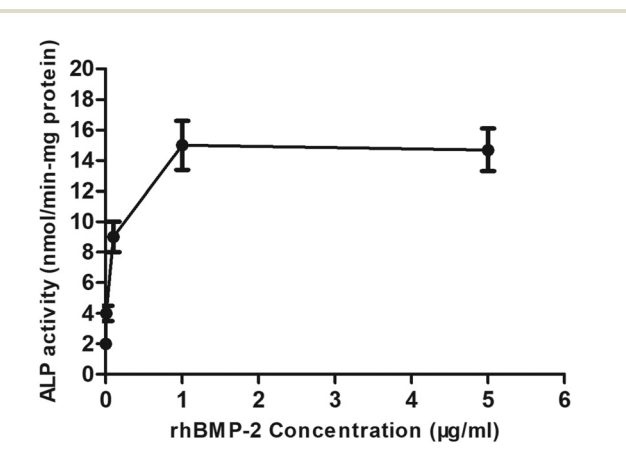


Fig. 2 rhBMP-2 facilitates the ALP activity of W20-17 cells in concentration dependence.

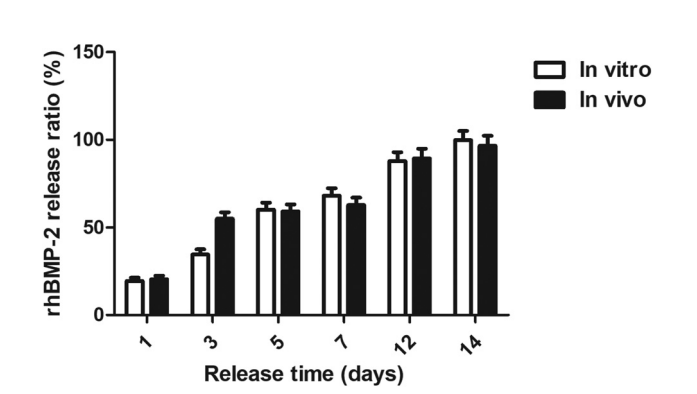


Fig. 3 In vitro and in vivo release kinetics of rhBMP-2 from the product.

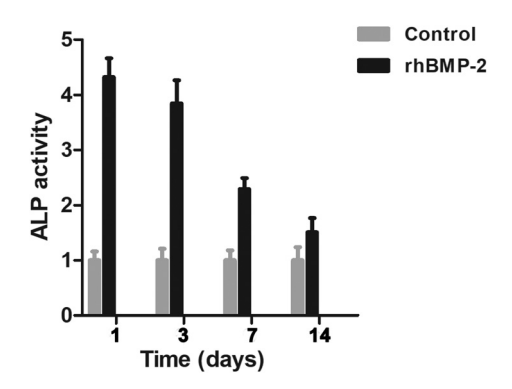


Fig. 4 The rhBMP-2 products increase ALP activity during the whole release process.

and released slowly until nearly all of the rhBMP-2 was released in fourteen days (Fig. 3).

#### Radiographic analyses

Fig. 5 presents the radiographical images of the control and rhBMP-2 groups. As indicated by the black arrow, a gap was evident within the 3D-AVI of the blank control group at the 50th day (Fig. 5A) and was non-existent in the rhBMP-2 group (Fig. 5B). Furthermore, the red arrows in Fig. 5B depict the newly formed bone around the 3D-AVI of the rhBMP-2 group, which is beneficial for early primary stability.

We observed the bone ingrowth directly through micro-CT. As shown in Fig. 5B, bone ingrowth from the posterior vertebral wall and both sides of the vertebral body was clearly observed.

Transverse-section CT images of the two groups are presented in Fig. 6 for evaluation of bone ingrowth.

Comparing Fig. 6A and C shows that the bone ingrowth of the rhBMP-2 group at the 50th day was significantly better than that of the control group. As indicated by the black arrow in Fig. 6C, the volume of bone ingrowth into the cavities at the center of the 3D-AVIs in the rhBMP-2 group was significantly higher than that of the control group. Consistent with the result on the 50th day, the bone ingrowth of the





Fig. 5 Lateral radiographical images of the blank control group and the rhBMP-2 group at the 50th day. (A) Lateral radiographical image of the blank control group. The black arrow indicates the gap within the 3D-AVI. (B) Lateral radiographical image of the rhBMP-2 group. Red arrows indicate the newly formed bone around the 3D-AVI.

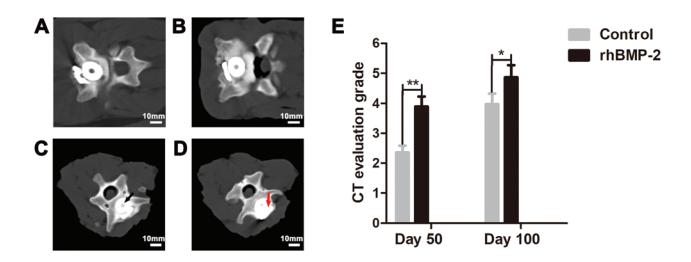


Fig. 6 Transverse section CT images of the blank control group at the 50th day (A) and the 100th day (B), and of the rhBMP-2 group at the 50th day (C) and the 100th day (D). The black arrow indicates the newly formed bone in the cavities at the center of 3D-AVIs of the control group. The red arrow indicates the gap between the fixed plate and the 3D-AVI, which disappears due to the newly formed bone. (E) The CT evaluation grade of the blank control group (grey) and the rhBMP-2 group (black) at the 50th (1) and 100th (2) days; \*\*p < 0.01, \*p < 0.05.

rhBMP-2 group at the 100th day was remarkably better than that of the control group. As indicated by the red arrow in Fig. 6C, the volume of bone ingrowth into the cavities at the center of the 3D-AVIs in the rhBMP-2 group was significantly greater than that of the control group, and the gap between the fixed plate and 3D-AVI disappeared due to the newly formed bone.

The CT evaluation grades of the two groups at the 50th and 100th days are presented in Fig. 6E. The CT evaluation grade of the rhBMP-2 group was significantly higher than that of the blank control group at the 50th day (p < 0.01) and the 100th day (p < 0.05). The above findings revealed that the added rhBMP-2 can accelerate the bone growth of 3D-AVIs.

#### Biomechanical stability

To investigate the effect of rhBMP-2 on the ROM of the cervical spines and the cervical spine stability, we conducted a series of biomechanical tests. As illustrated in Fig. 7, there was a significant difference in the ROM of flexion and extension, bending, and rotation between the two groups (p < 0.01). Specifically, the results suggested that rhBMP-2 reduced the ROM of the cervical spines to some extent while strengthening the cervical spine stability.

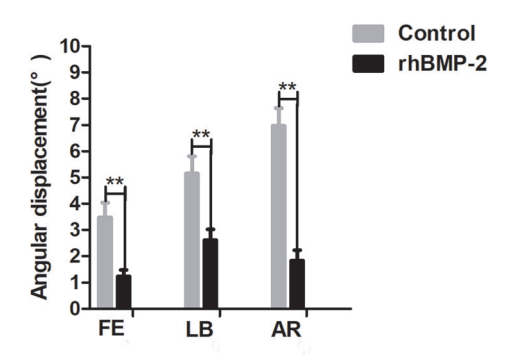


Fig. 7 Comparison of a range of motions of C2-C6 segments in the flexion-extension (FE, 1), lateral bending (LB, 2) and axial rotation (AR, 3) motion planes; \*\*p < 0.01.

#### Osseointegration evaluation by micro-CT

To explore the effect of rhBMP-2 on the in vivo osseointegration of porous 3D-AVIs, we quantified the bone formation both around the scaffold and within it by micro-CT analysis. As illustrated in Fig. 8A and B, the Ti alloy, bones in the periimplant region, and bones within the 3D-AVIs were labelled white, green, and pink, respectively. In an overall view, the rhBMP-2 group had more bone formation in both regions. The quantitative analysis results of the bone fraction at the periimplant and intraporous region of the 3D-AVIs are presented in Fig. 8C. The bone fraction at the peri-implant (p < 0.05) and intraporous region (p < 0.01) was significantly higher in the rhBMP-2 group.

Furthermore, 3D reconstruction images confirmed that the osseointegration of the porous 3D-AVIs in the rhBMP-2 group was better than that of the control group (Fig. 8D and E). Hence, the added rhBMP-2 enhances bone ingrowth as well as bone on-growth at the porous 3D-AVIs.

#### Osseointegration evaluated by fluorescence labelling

Osseointegration efficiency. The fluorescence labelling further illustrated the osseointegration efficiency of the 3D-AVIs. As shown in Fig. 9, the green and red bands denote the newly formed bone stained by calcein green and tetracycline, respectively. Based on the comparison between Fig. 9B and D, we can infer that the osseointegration efficiency around the 3D-AVIs was similar for the two groups. However, the comparison between Fig. 9A and C clearly demonstrates the superior osseointegration efficiency inside the pores of the rhBMP-2 group.

Osseointegration direction. Apart from osseointegration efficiency, the direction of osseointegration can also be revealed by fluorescence labelling. In contrast to the results

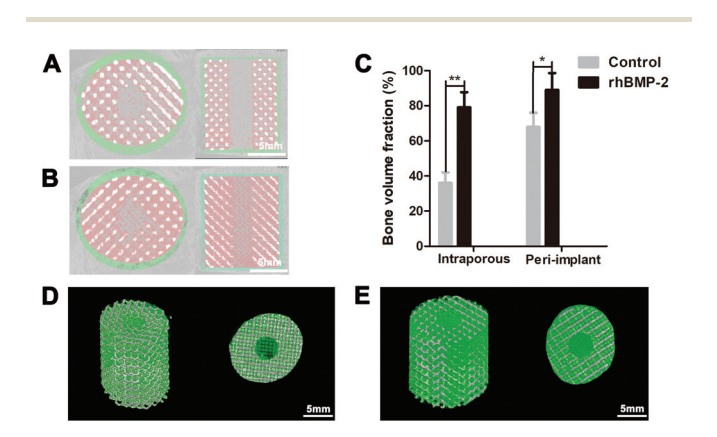


Fig. 8 Micro-CT images of 3D-AVIs of the control (A) and rhBMP-2 (B) groups 100 days after in vivo implantation. Ti, bones in the peri-implant region, and those within the 3D-AVIs are labelled white, green, and pink, respectively. (C) Quantitative results of bone fractions in the periimplant region and intraporous region of the 3D-AVIs in the control (grey) and rhBMP-2 (black) groups; p < 0.05, p < 0.01 (p = 4 per group). Three-dimensional reconstruction images of the control and rhBMP-2 groups at the 100th day after implantation. (D) Side and top views of the control group, (E) side and top views of the rhBMP-2 group.

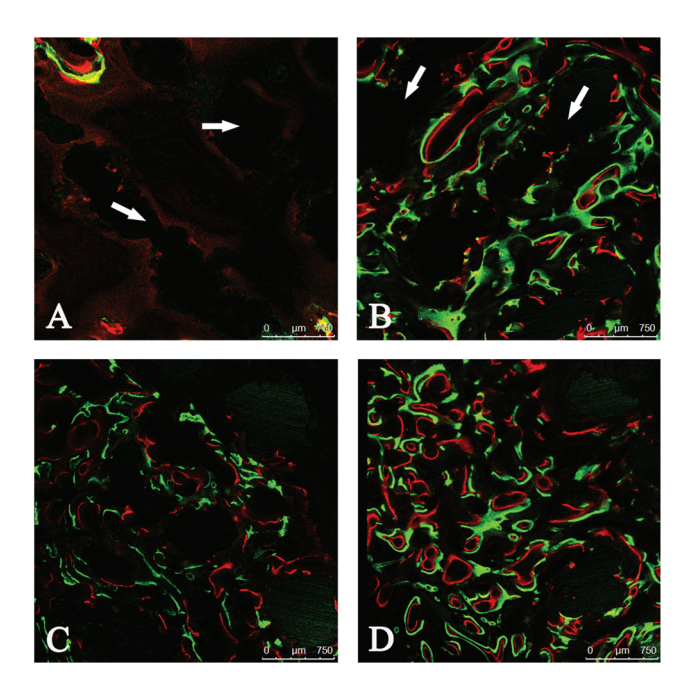


Fig. 9 Representative fluorescent micrographs of the control and rhBMP-2 groups. (A) Inside the pores (white arrows) of the 3D-AVIs of the control group. (B) Inside the pores (white arrows) of the 3D-AVIs of the rhBMP-2 group. Region around the 3D-AVIs of (C) the control group and (D) the rh-BMP-2 group.

summarized above, the osseointegration directions of the two groups were the same. The newly formed bone marked by calcein green emits green fluorescence excited by blue light, as indicated by the red arrow in Fig. 10A, whereas the newly formed bone marked by tetracycline emits yellow fluorescence excited by purple light. Fig. 10A and B show representative fluorescence micrographs around the 3D-AVIs, and Fig. 10C and D show representative fluorescent micrographs inside the pores of 3D-AVIs (the white arrow indicates the Ti beside the pores). Hence, from a macroview, bone tissue grew from the periphery to the center of the 3D-AVIs, as indicated by the black arrows in Fig. 10E and F. Moreover, the microview images shown in Fig. 10G and H demonstrated that the bone tissue first grew into the pore space and then interlocked with the Ti surface.

#### Histologic analysis

Fig. 11 shows the representative histological images of 3D-AVIs in the cervical corpectomy bone defects in which the struts of the Ti are displayed in black, while newly formed bones are red. For the control group, only the peripheral area and cavities at the centre of the 3D-AVIs were filled with mineralized bones, whereas the quantity of intraporous ingrown bone was barely satisfactory (Fig. 11A). In contrast, bone growth in the rhBMP-2 group was more extensive and homogeneously distributed both at the peripheral area and in the intraporous region, appearing as though nearly every strut of Ti was filled with bones (Fig. 11B). Fig. 11E shows a significantly higher

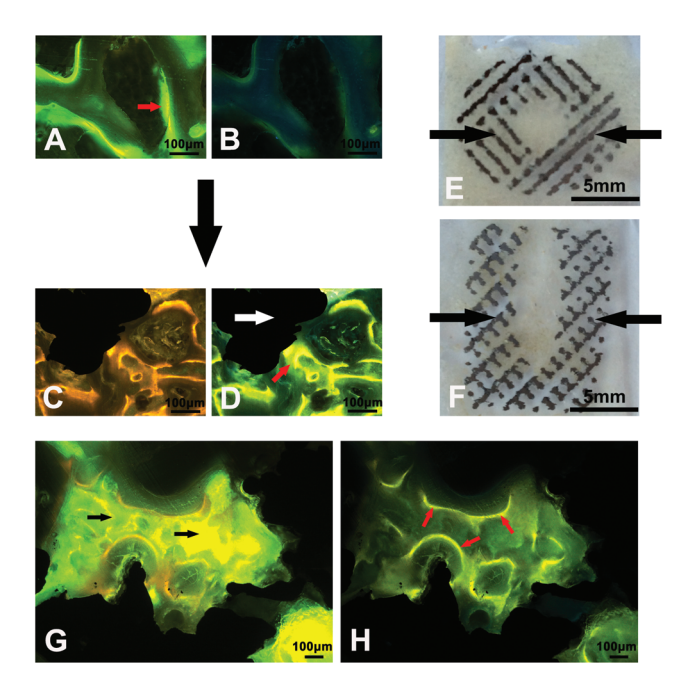


Fig. 10 Fluorescence labelling (representative fluorescent micrographs) revealing the osseointegration direction of the 3D-AVIs in the control and rhBMP-2 group from a macroperspective (5x magnification) and within the pores of the 3D-AVIs (10x magnification). (A) Around the 3D-AVI excited by blue light. The red arrow indicates the newly formed bone after calcein green injection. (B) Around the 3D-AVI excited by purple light. (C) Around the 3D-AVI excited by blue light. (D) Around the 3D-AVI excited by purple light. The red arrow indicates the newly formed bone after tetracycline injection 18 days after calcein green injection. (E) Transverse histological section of a 3D-AVI; the black arrows indicate the osseointegration direction. (F) Longitudinal histological section of a 3D-AVI; the black arrows indicate the osseointegration direction. (G) Within the pore of the 3D-AVI excited by blue light. The black arrow indicates the newly formed bone after calcein green injection. (H) Within the pore of the 3D-AVI excited by purple light. The red arrow indicates the newly formed bone after tetracycline injection 18 days after calcein green injection.

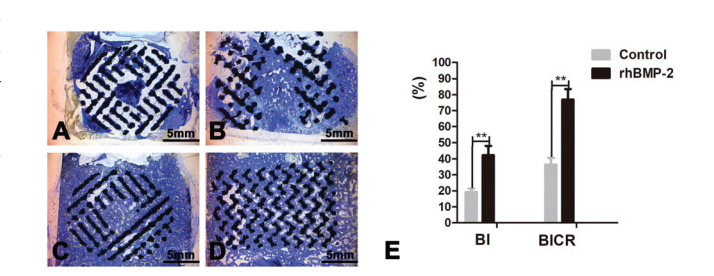


Fig. 11 Histological staining of the (A) transverse and (B) longitudinal section of the 3D-AVI in the control group, and of the (C) transverse and (D) longitudinal section of the 3D-AVI in the rhBMP-2 group (n=10 per group). (E) Quantitative results of bone in-growth (BI) and bone-implant contact ratio (BICR) of the 3D-AVI in the two groups; \*\*p < 0.01 (n=10 per group).

bone ingrowth and bone-implant contact ratio at the 3D-AVIs in the rhBMP-2 group, representing a 120% and 111% increase compared to those of the control group, respectively (p < 0.05).

#### Discussion

Osteoconduction and osteoinduction are considered to be the most crucial parameters for evaluating the quality of artificial implants for the reconstruction of large bone defects. 8,9 Despite extensive effort to solve this problem, including the use of autologous skeletal stem cells and surface modifications, 14,32,33 these methods either have a complex preparation process or a limited osseointegration effect, with some even causing further surgical trauma. In this study, we established and validated a simple and effective approach to enhance the osseointegration of the 3D-printed porous Ti6Al4V implant by combining rhBMP-2 with a specially designed 3D-printed porous Ti6Al4V vertebral implant.

Our proposed method greatly improved the osseointegration effect and bone formation efficiency of the 3D-printed porous Ti6Al4V implant. As revealed by the radiographic test, more newly formed bone appear around and inside the 3D-AVIs at the 50th and 100th day, demonstrating that our method could achieve earlier and more stable fixation, which would allow for even elderly patients to realize earlier self-care, work, and sport. BMP-2 is currently the only FDA-approved osteoinductive growth factor that is used as a bone graft substitute. In general, BMP-2 RNA expression in osteoblast and cartilage cells is evident at five to eleven days after bone fracture. 34,35 The in vitro release process of BMP-2 in the present study exhibited two time phases, burst release and slow stable release; 40% BMP-2 was released in the first three days, and 70% BMP-2 was released in the first week. Almost 100% of the BMP-2 was released by the 14th day. Hence, the release of BMP-2 in the present study basically conformed to the in vivo BMP-2 release characteristic, and perfectly meets the needs of bone growth.

Hydroxyapatite has obvious advantages as an osteoconductive matrix as well as a carrier material for BMP2-like bone growth factor delivery. Furthermore, phospholipid prolongs the time of BMP-2 to some extent. Undoubtedly, in the present study, rhBMP-2 loaded in hydroxyapatite and phospholipid for sustained release greatly contributed to the enhancement in new bone formation. In addition, the designed cavity at the center of the cylindrical 3D-AVI becomes a relatively confined space after surgery, which could also prolong BMP-2 release. Notably, the use of infusion in human cervical spine surgery has been shown to significantly increase the incidence of post-operative dysphagia. However, we did not observe any differences in post-operative eating habits between the two groups of sheep, which could indicate swallowing and/or upper gastrointestinal tract issues.

In summary, under the precondition of an appropriate dose, the early use of rhBMP-2 appears to be favourable for osseointegration enhancement of 3D-AVIs. There are several potential mechanisms to explain how BMP2 enhances osseointegration. At the genetic level, Noda *et al.*<sup>42</sup> reported that BMP-2 enhanced the expression level of the *Lgr4* gene in osteoblastic cells, and Zhou *et al.*<sup>43</sup> reported that BMP2 induces chondrogenic differentiation, osteogenic differentiation, and endochondral ossification in stem cells. More recently, Yu

*et al.*<sup>44</sup> identified the BMP2-correlation networks during fracture healing, including 26 differentially expressed genes. Some researchers have also studied the BMP2 signalling pathway of senile osteoporotic fracture healing.<sup>45</sup>

Our proposed approach is similar to that of Lv et al., 23 who incorporated BMP2 in porous Ti6Al4V scaffolds with doped fibrin glue. Nonetheless, the osseointegration effect of our present method was superior to that obtained in the previous study, and the present method is more convenient and feasible. Unlike the complex and multi-step treatment required with fibrin glue, our method only requires insertion of rhBMP-2 into prepared cavities in the 3D-AVI at the time of surgery. 16 Moreover, the bone ingrowth of the control group was in line with that reported in several previous studies. For example, the bone ingrowth of EBM porous Ti at the frontal skull of pigs was reported to be 30% and 46% at 30 and 60 days, respectively.46 Previous long-term studies of the osseointegration of porous Ti in a sheep model also demonstrated a significantly higher bone-implant contact ratio compared with that obtained in the current study. 47,48

Although we did not observe any clear non-union at the time of sacrifice (100 days) in the control group, virtually all of the present results demonstrate that rhBMP-2 not only enhanced the osseointegration effect but also accelerated the bone formation efficiency, indicating that the benefits gained may ensure earlier and more stable fixation, thereby reducing the risk of various surgical complications. Most notably, this method should be feasible for more difficult cases such as the repair of large or complicated bone defects, or in cases of low osteogenic capability. 49 Furthermore, to our knowledge, this is the first study to investigate the osseointegration directions around and inside 3D-printed porous Ti6Al4V implants with or without rhBMP-2. In brief, this work offers a convenient intraoperative approach to achieve earlier and more stable fixation when using 3D-printed porous Ti6Al4V implants. With the help of rhBMP-2, the application range of these implants can be further expanded.

However, some drawbacks of the present study are worth noting. Although we identified the beneficial effect of this novel and intraoperative approach for improving the osseointegration of 3D-printed porous Ti6Al4V implants, the appropriate dosage remains to be determined to avoid postoperative inflammation and associated adverse effects, including ectopic bone formation or osteoclast-mediated bone resorption. April BMP-2 has also been reported to be linked to tumorigenesis. Hence, caution must be taken to optimize the rhBMP-2 dosage in clinical applications. Moreover, our results are encouraging in sheep, but require further validation in patients. Therefore, future work should focus on the exploration of BMP-2 dosage and its clinical validation to promote the practical feasibility of this method.

#### Conclusions

We successfully improved the osseointegration of a 3D-AVI by loading rhBMP-2 into a cavity designed at the center of the

implant intraoperatively. Radiographic, biomechanical, micro-CT, fluorescence labelling, and histologic tests were systematically performed to investigate the osseointegration of the 3D-AVI on a cervical corpectomy bone defect model in sheep. In comparison with the blank control group, the rhBMP-2 group showed remarkable enhancement in osseointegration capacity. Furthermore, osseointegration direction assessments demonstrated bone tissue growth from the periphery to the center of the 3D-AVIs, beginning with growth into the pore space and then ultimately interlocking with the Ti surface.

#### Conflicts of interest

There are no conflicts of interest to declare.

### Acknowledgements

The authors acknowledge the grant from the Ministry of Science and Technology of China (no. 2016YFB1101501) and research and financial support from the Beijing AKEC Medical Co., Ltd.

#### References

- 1 K. Zhao, Y. Wang, M. Lu, K. Yao, C. Xiao, Y. Zhou, L. Min, Y. Luo and C. Tu, Progress in repair and reconstruction of large segmental bone tumor defect in distal tibia, *Chin. J. Repar. Reconstr. Surg.*, 2018, 32, 1211–1217.
- 2 P. F. Horstmann, W. H. Hettwer and M. M. Petersen, Treatment of benign and borderline bone tumors with combined curettage and bone defect reconstruction, *J. Orthop. Surg.*, 2018, 3, 1–7.
- 3 H. Al Husaini, P. Wheatley-Price, M. Clemons and F. A. Shepherd, Prevention and management of bone metastases in lung cancer: a review, *J. Thorac. Oncol.*, 2009, 4, 251–259.
- 4 R. Ahmad, I. Ahmad, R. Akram, A. U. Zaman and A. Aziz, Cage displacement after anterior decompression and interbody titanium mesh cage placement in caries spine, *Pak. J. Med. Health Sci.*, 2016, **10**, 730–733.
- 5 K. Sun, J. Sun, S. Wang, X. Xu, Y. Wang, T. Xu, H. Zhao and J. Shi, Placement of titanium mesh in hybrid decompression surgery to avoid graft subsidence in treatment of three-level cervical spondylotic myelopathy: cephalad or caudal?, *Med. Sci. Monit.*, 2018, 24, 9479–9487.
- 6 W. B. Du, L. X. Wang, F. X. Shen, G. M. Wu, L. Xu and R. F. Quan, Application of drilling columnar autogenous iliac bone graft and clinical analysis of postoperative complications in the donor bone region, *Zhongguo Gushang*, 2018, 31, 446–451.
- 7 N. Xu, F. Wei, X. Liu, L. Jiang, H. Cai, Z. Li, M. Yu, F. Wu and Z. Liu, Reconstruction of the upper cervical spine

- using a personalized 3D-printed vertebral body in an adolescent with Ewing sarcoma, *Spine*, 2016, 1, 50–54.
- 8 T. Albrektsson and C. Johansson, Osteoinduction, osteoconduction and osseointegration, *Eur. Spine J.*, 2001, **10**, 96–101.
- 9 E. A. Lewallen, S. M. Riester, C. A. Bonin, H. M. Kremers, A. Dudakovic, S. Kakar, R. C. Cohen, J. J. Westendorf, D. G. Lewallen and A. J. van Wijnen, Biological strategies for improved osseointegration and osteoinduction of porous metal orthopedic implants, *Tissue Eng., Part B*, 2015, 21, 218–230.
- 10 P. Zhang, X. Wang, Z. Lin, H. Lin, Z. Zhang, W. Lin, X. Yang and J. Cui, Ti-based biomedical material modified with TiOx/TiNx duplex bioactivity film via micro-arc oxidation and nitrogen ion implantation, *Nanomaterials*, 2017, 7, 1–12.
- 11 M. Chamseddine, S. Breden, M. F. Pietschmann, P. E. Müller and Y. Chevalier, Periprosthetic bone quality affects the fixation of anatomic glenoids in total shoulder arthroplasty: in vitro study, *J. Shoulder Elb. Surg.*, 2019, **28**, 18–28.
- 12 R. Verboket, M. Leiblein, C. Seebach, C. Nau, M. Janko, M. Bellen, H. Bönig, D. Henrich and I. Marzi, Autologous cell-based therapy for treatment of large bone defects: from bench to bedside, *Eur. J. Trauma Emerg. Surg.*, 2018, 44, 649–665.
- 13 Y. Watanabe, N. Harada, K. Sato, S. Abe, K. Yamanaka and T. Matushita, Stem cell therapy: is there a future for reconstruction of large bone defects?, *Injury*, 2016, 47, 47–51.
- 14 P. Xiu, Z. Jia, J. Lv, C. Yin, Y. Cheng, K. Zhang, C. Song, H. Leng, Y. Zheng, H. Cai and Z. Liu, Tailored surface treatment of 3D printed porous Ti6Al4V by microarc oxidation for enhanced osseointegration via optimized bone ingrowth patterns and interlocked bone/implant interface, ACS Appl. Mater. Interfaces, 2016, 8, 17964–17975.
- 15 J. P. Govindharajulu, X. Chen, Y. Li, J. C. Rodriguez-Cabello, M. Battacharya and C. Aparicio, Chitosan-recombinamer layer-by-layer coatings for multifunctional implants, *Int. J. Mol. Sci.*, 2017, **18**, 1–16.
- 16 M. Mi, H. Jin, B. Wang, K. Yukata, T. J. Sheu, Q. H. Ke, P. Tong, H. J. Im, G. Xiao and D. Chen, Chondrocyte BMP2 signaling plays an essential role in bone fracture healing, *Gene*, 2013, 512, 211–218.
- 17 R. De la Garza Ramos, J. Nakhla, M. Echt, Y. Gelfand, D. J. Altschul, W. Cho, M. d. Kinon and R. Yassari, Use of bone morphogenetic protein-2 in vertebral column tumor surgery: a national investigation, *World Neurosurg.*, 2018, 117, 17–21.
- 18 T. J. Myers, L. Longobardi, H. Willcockson, J. D. Temple, L. Tagliafierro, P. Ye, T. Li, A. Esposito, B. M. Moats-Staats and A. Spagnoli, BMP2 regulation of CXCL12 cellular, temporal, and spatial expression is essential during fracture repair, *J. Bone Miner. Res.*, 2015, 30, 2014–2027.
- 19 M. Murnaghan, L. McIlmurray, M. T. Mushipe and G. Li, Time for treating bone fracture using rhBMP-2: a randomised placebo controlled mouse fracture trial, *J. Orthop. Res.*, 2005, 23, 625–631.

20 W. G. La, S. W. Kang, H. S. Yang, S. H. Bhang, S. H. Lee, J. H. Park and B. S. Kim, The efficacy of bone morphogenetic protein-2 depends on its mode of delivery, *Artif. Organs*, 2010, 34, 1150–1153.

- 21 S. Srouji, D. Ben-David, R. Lotan, E. Livne, R. Avrahami and E. Zussman, Slow-release human recombinant bone morphogenetic protein-2 embedded within electrospun scaffolds for regeneration of bone defect: in vitro and in vivo evaluation, *Tissue Eng.*, *Part A*, 2011, 17, 269–277.
- 22 M. S. Ghiasi, J. Chen, A. Vaziri, E. K. Rodriguez and A. Nazarian, Bone fracture healing in mechanobiological modeling: A review of principles and methods, *Bone Rep.*, 2017, **6**, 87–100.
- 23 J. Lv, P. Xiu, J. Tan, Z. Jia, H. Cai and Z. Liu, Enhanced angiogenesis and osteogenesis in critical bone defects by the controlled release of BMP-2 and VEGF: implantation of electron beam melting-fabricated porous Ti6al4v scaffolds incorporating growth factor-doped fibrin glue, *Biomed. Mater.*, 2015, 3, 035013.
- 24 R. K. Siu, S. S. Lu, W. Li, J. Whang, G. McNeill, X. Zhang, B. M. Wu, A. S. Turner, H. B. Seim 3<sup>rd</sup>, P. Hoang, J. C. Wang, A. A. Gertzman, K. Ting and C. Soo, Nell-1 protein promotes bone formation in a sheep spinal fusion model, *Tissue Eng.*, *Part A*, 2011, 17, 1123–1135.
- 25 S. Valentin, T. F. Licka and J. Elliott, MRI-determined lumbar muscle morphometry in man and sheep: potential biomechanical implications for ovine model to human spine translation, *J. Anat.*, 2015, 227, 506–513.
- 26 M. G. Axelsen, S. Overgaard, S. M. Jespersen and M. Ding, Comparison of synthetic bone graft ABM/P-15 and allograft on uninstrumented posterior lumbar spine fusion in sheep, *J. Orthop. Surg. Res.*, 2019, **14**, 2.
- 27 L. Wang, Y. Wang, L. Shi, P. Liu, J. Kang, J. He, Y. Liu and D. Li, Can the sheep model fully represent the human model for the functional evaluation of cervical interbody fusion cages?, *Biomech. Model Mechanobiol.*, 2018, 18, 1–10.
- 28 E. Truumees, C. K. Demetropoulos, K. H. Yang and H. N. Herkowitz, Effects of disc height and distractive forces on graft compression in an anterior cervical corpectomy model, *Spine*, 2008, 33, 1438–1441.
- 29 L. Chen, H. L. Liu, Y. Gu, Y. Feng and H. L. Yang, Lumbar interbody fusion with porous biphasic calcium phosphate enhanced by recombinant bone morphogenetic protein-2/silk fibroin sustained-released microsphere: an experimental study on sheep model, *J. Mater. Sci. Mater. Med.*, 2015, 26, 126.
- 30 J. Yang, H. Cai, J. Lv, K. Zhang, H. Leng, C. Sun, Z. Wang and Z. Liu, In vivo study of a self-stabilizing artificial vertebral body fabricated by electron beam melting, *Spine*, 2014, **8**, 486–492.
- 31 S. M. van Gaalen, M. C. Kruyt, R. E. Geuze, J. D. de Bruijn, J. Alblas and W. J. Dhert, Use of fluorochrome labels in in vivo bone tissue engineering research, *Tissue Eng., Part B*, 2010, **16**, 209–217.
- 32 R. Verboket, M. Leiblein, C. Seebach, C. Nau, M. Janko, M. Bellen, H. Bönig, D. Henrich and I. Marzi, Autologous

- cell-based therapy for treatment of large bone defects: from bench to bedside, *Eur. J. Trauma Emerg. Surg.*, 2018, **44**, 649–665.
- 33 Y. Watanabe, N. Harada, K. Sato, S. Abe, K. Yamanaka and T. Matushita, Stem cell therapy: is there a future for reconstruction of large bone defects?, *Injury*, 2016, 47, S47–S51.
- 34 Y. Hara, M. Ghazizadeh, H. Shimizu, H. Matsumoto, N. Saito, T. Yagi, K. Mashiko, K. Mashiko, M. Kawai and H. Yokota, Delayed expression of circulating TGF-β1 and BMP-2 levels in human nonunion long bone fracture healing, *J. Nippon Med. Sch.*, 2017, **84**, 12–18.
- 35 K. Tsuji, A. Bandyopadhyay, B. D. Harfe, K. Cox, S. Kakar, L. Gerstenfeld, T. Einhorn, C. J. Tabin and V. Rosen, BMP2 activity, although dispensable for bone formation, is required for the initiation of fracture healing, *Nat. Genet.*, 2006, 38, 1424–1429.
- 36 M. Hasegawa, T. A. Kudo, H. Kanetaka, T. Miyazaki, M. Hashimoto and M. Kawashita, Fibronectin adsorption on osteoconductive hydroxyapatite and non-osteoconductive α-alumina, *Biomed. Mater.*, 2016, 11, 045006.
- 37 E. Ahmadzadeh, F. Talebnia, M. Tabatabaei, H. Ahmadzadeh and B. Mostaghaci, Osteoconductive composite graft based on bacterial synthesized hydroxyapatite nanoparticles doped with different ions: From synthesis to in vivo studies, *Nanomedicine*, 2016, 12, 1387–1395.
- 38 L. Xiong, J. Zeng, A. Yao, Q. Tu, J. Li, L. Yan and Z. Tang, BMP2-loaded hollow hydroxyapatite microspheres exhibit enhanced osteoinduction and osteogenicity in large bone defects, *Int. J. Nanomed.*, 2015, **10**, 517–526.
- 39 J. K. Cha, J. S. Lee, M. S. Kim, S. H. Choi, K. S. Cho and U. W. Jung, Sinus augmentation using BMP-2 in a bovine hydroxyapatite/collagen carrier in dogs, *J. Clin. Periodontol.*, 2014, 41, 86–93.
- 40 X. Peng, Y. Chen, Y. Li, Y. Wang and X. Zhang, A long-acting BMP-2 release system based on poly (3-hydroxybuty-rate) nanoparticles modified by amphiphilic phospholipid for osteogenic differentiation, *BioMed. Res. Int.*, 2016, 2016, 5878645
- 41 B. D. Riederman, B. A. Butler, C. D. Lawton, B. D. Rosenthal, E. S. Balderama and A. J. Bernstein, Recombinant human bone morphogenetic protein-2 versus iliac crest bone graft in anterior cervical discectomy and fusion: Dysphagia and dysphonia rates in the early post-operative period with review of the literature, *J. Clin. Neurosci.*, 2017, 44, 180–183.
- 42 C. Pawaputanon Na Mahasarakham, Y. Ezura, M. Kawasaki, A. Smriti, S. Moriya, T. Yamada, Y. Izu, A. Nifuji, K. Nishimori, Y. Izumi and M. Noda, BMP-2 enhances Lgr4 gene expression in osteoblastic cells, *J. Cell Physiol.*, 2016, 231, 887–895.
- 43 N. Zhou, Q. Li, X. Lin, N. Hu, J. Y. Liao, L. B. Lin, C. Zhao, Z. M. Hu, X. Liang, W. Xu, H. Chen and W. Huang, BMP2 induces chondrogenic differentiation, osteogenic differentiation and endochondral ossification in stem cells, *Cell Tissue Res.*, 2016, 366, 101–111.

44 Y. H. Yu, K. Wilk, P. L. Waldon and G. Intini, In vivo identification of Bmp2-correlation networks during fracture healing by means of a limb-specific conditional inactivation of BMP2, *Bone*, 2018, **116**, 103–110.

- 45 D. B. Liu, C. Sui, T. T. Wu, L. Z. Wu, Y. Y. Zhu and Z. H. Ren, Association of bone morphogenetic protein (BMP)/Smad signaling pathway with fracture healing and osteogenic ability in senile osteoporotic fracture in humans and rats, *Med. Sci. Monit.*, 2018, 24, 4363–4371.
- 46 S. Ponader, C. von Wilmowsky, M. Widenmayer, R. Lutz, P. Heinl, C. Körner, R. F. Singer, E. Nkenke, F. W. Neukam and K. A. Schlegel, In vivo performance of selective electron beam-melted Ti-6al-4v structures, *J. Biomed. Mater. Res.*, *Part A*, 2010, **92**, 56–62.
- 47 F. A. Shah, O. Omar, F. Suska, A. Snis, A. Matic, L. Emanuelsson, B. Norlindh, J. Lausmaa, P. Thomsen and A. Palmquist, Long-term osseointegration of 3D printed Cocr constructs with an interconnected open-pore architecture prepared by electron beam melting, *Acta Biomater.*, 2016, 36, 296–309.
- 48 F. A. Shah, A. Snis, A. Matic, P. Thomsen and A. Palmquist, 3D printed Ti6Al4V implant surface promotes bone maturation and retains a higher density of less aged osteocytes

- at the bone-implant interface, Acta Biomater., 2016, 30, 357–367
- 49 A. W. James, G. LaChaud, J. Shen, G. Asatrian, V. Nguyen, X. Zhang, K. Ting and C. Soo, A review of the clinical side effects of bone morphogenetic protein-2, *Tissue Eng., Part B*, 2016, 22, 284–297.
- 50 V. Nguyen, C. A. Meyers, N. Yan, S. Agarwal, B. Levi and A. W. James, BMP-2-induced bone formation and neural inflammation, *J. Orthop.*, 2017, 14, 252–256.
- 51 Z. Q. Hong, L. M. Tao and Z. X. Bin, Differentiation of osteoblast-like cells and ectopic bone formation induced by bone marrow stem cells transfected with chitosan nanoparticles containing plasmid-BMP2 sequences, *Mol. Med. Rep.*, 2017, **15**, 1353–1361.
- 52 H. Tian, J. Zhao, E. J. Brochmann, J. C. Wang and S. S. Murray, Bone morphogenetic protein-2 and tumor growth: diverse effects and possibilities for therapy, *Cytokine Growth Factor Rev.*, 2017, **34**, 73–91.
- 53 M. H. Wang, X. M. Zhou, M. Y. Zhang, L. Shi, R. W. Xiao, L. S. Zeng, X. Z. Yang, X. F. S. Zheng, H. Y. Wang and S. J. Mai, BMP2 promotes proliferation and invasion of nasopharyngeal carcinoma cells via mTORC1 pathway, *Aging*, 2017, 9, 1326–1340.